



Mid-infrared second-harmonic generation in ultra-thin plasmonic metasurfaces without a full-metal backplane

Nishant Nookala¹ · Jiaming Xu¹ · Omri Wolf^{2,3} · Stephen March¹ · Raktim Sarma^{2,3} · Seth Bank¹ · John Klem³ · Igal Brener^{2,3} · Mikhail Belkin¹

Received: 22 February 2018 / Accepted: 6 June 2018
© Springer-Verlag GmbH Germany, part of Springer Nature 2018

Abstract

We report the design and operation of a nonlinear intersubband polaritonic metasurface for mid-infrared second harmonic generation. The metasurface is made of plasmonic nanoresonators filled with a multiple-quantum-well semiconductor heterostructure. Unlike the previously reported nonlinear intersubband polaritonic metasurfaces that employ full-metal backplanes below the etched metal–semiconductor nanoresonators, the metasurface reported here employs an incomplete backplane that is complementary to the pattern of the top metallization of the etched semiconductor heterostructure nanoresonators. The new approach produces high-electric-field localization and enhancement in the nanoresonators, while requiring simplified fabrication and allowing the metasurface to operate in both transmission and reflection regimes.

1 Introduction

Recent interest in enhancing optical nonlinearities has unveiled a host of promising engineered designs beyond conventionally used bulk crystals, including novel waveguiding schemes [1, 2], micro-cavity-based approaches [3], and metallic nanoantenna arrays [4]. In particular, metasurface-based flat optical components have been put forward to achieve a variety of exotic linear and nonlinear effects, potentially replacing bulky three-dimensional analogues with more compact and versatile two-dimensional equivalents with sub-wavelength thickness [5–9]. The field of nonlinear optics can benefit greatly from the introduction of sub-wavelength thickness nonlinear metasurfaces to provide efficient nonlinear frequency mixing without the

phase-matching constraints of bulk nonlinear crystals [10] and with the ability to control the phase front of the output beam [9, 11–13].

To achieve efficient frequency mixing in films of sub-wavelength thickness using pumping intensities below the materials' damage thresholds, metasurfaces need to have nonlinear susceptibility several orders of magnitude larger than that of natural nonlinear crystals [8]. Nonlinear intersubband polaritonic metasurfaces [7, 8, 13] currently provide the largest second-order nonlinear response of all metasurfaces demonstrated so far. They consist of plasmonic nanoresonators filled with multiple-quantum well (MQW) semiconductor heterostructures designed to possess giant nonlinear response associated with intersubband transitions, as shown in an example in Fig. 1. Such metasurfaces can be designed for operation anywhere in the mid-infrared (mid-IR) spectral range (3–30 μm wavelength) [8, 13, 14] as well as at near-infrared wavelengths [14], and can achieve continuous phase control over the nonlinearly generated beams [9, 13, 15], presenting an effective case for the platform to pioneer a path towards the realization of efficient, flat nonlinear optical elements.

Recently, we reported a nonlinear polaritonic metasurface that exhibits what we believe to be the largest value for second-order nonlinear susceptibility for second-harmonic generation (SHG) in the mid-IR spectral range of $1.2 \times 10^6 \text{ pm V}^{-1}$ [8], which is 3–6 orders of magnitude larger than that of traditional nonlinear optical crystals [10, 16] as

This article is part of the topical collection “Mid-infrared and THz Laser Sources and Applications” guest edited by Wei Ren, Paolo De Natale, and Gerard Wysocki.

✉ Mikhail Belkin
mbelkin@ece.utexas.edu

¹ Department of Electrical and Computer Engineering, University of Texas at Austin, Austin, TX 78758, USA

² Center for Integrated Nanotechnologies, Sandia National Laboratories, P.O. Box 5800, Albuquerque, NM 87185, USA

³ Sandia National Laboratories, P.O. Box 5800, Albuquerque, NM 87185, USA

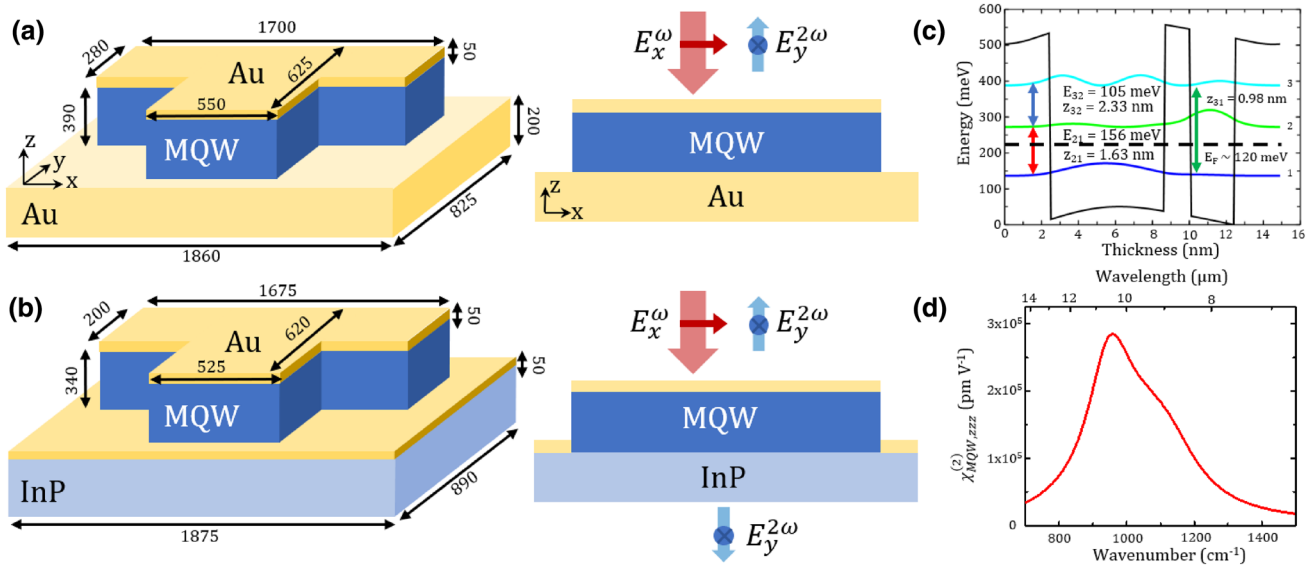


Fig. 1 **a** Graphic perspective (*l*) and side (*r*) views of one unit cell of a second harmonic generating metasurface with a full-metal backplane; dimensions given in nm. **b** Same as **a**, but showing the unit cell of our proposed “incomplete-metal backplane” nonlinear metasurface. **c** Conduction band diagram of one period of an $\text{In}_{0.53}\text{Ga}_{0.47}\text{As}/\text{Al}_{0.48}\text{In}_{0.52}\text{As}$ -coupled quantum well structure designed for giant second-harmonic nonlinear response. Shown are the electron energy lev-

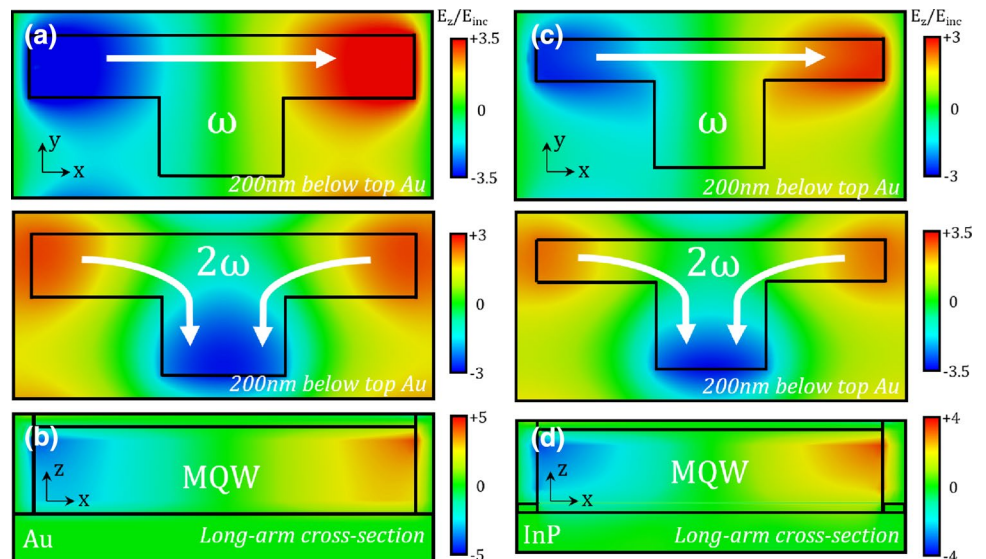
els and the square of electron states wavefunctions, measured energy transitions, and calculated transition dipole moments, z_{ij} , between states i and j . Also shown is the room-temperature Fermi energy (E_F). **d** Calculated intersubband second-order nonlinear susceptibility for the structure in **c** as a function of pump frequency

well as nonlinear metasurfaces reported earlier [11, 12, 17, 18]. We experimentally demonstrated SHG power conversion efficiency of 0.075% with this metasurface, which was only $\lambda/25$ in thickness, at a pump wavelength of $10\ \mu\text{m}$ [8].

These metasurfaces were based on an array of metal–MQW–metal nanoresonators, shown in Fig. 1a. The metallic resonators are designed to resonantly couple the x -polarized fundamental-frequency (FF) wave from

free-space and produce a strong z -polarized electric field component normal to the surface at the metal–MQW nanocavity, as shown in Fig. 2. z -polarized electric field at the pump frequency couples to the intersubband transitions in the MQW and produces a z -polarized nonlinear polarization oscillating at the second-harmonic (SH) frequency. The polarization couples to the second-harmonic nanocavity resonance as shown in Fig. 2 and radiates y -polarized

Fig. 2 Numerical simulations of the plasmonic nonlinear metasurfaces under study. **a** Top-down view (200 nm below the top gold) of the E_z field distribution (normalized to the field amplitude E_{inc} on the normally incident excitation plane wave) in the etched-T full-metal-backplane geometry for pump and second-harmonic frequencies. **b** Side view of the normalized E_z field distribution along a middle cross section of the x -aligned arm of the T-structure. **c–d** Same as **a**, **b** but for the incomplete-metal backplane geometry discussed in this work



radiation to free space. This approach allows for the efficient coupling of the optical fields of the incoming and outgoing waves normal to the metasurface with z -polarized intersubband transitions in the MQW heterostructure and further enhances the already large nonlinear susceptibility of the MQW [7, 8].

A metal backplane underneath the MQW resonators was the key element of the metasurface design in Ref. [4] that allowed us to produce high and uniform field enhancement in the MQW layers that resulted in the record metasurface performance. The MQW layer was transferred onto a layer of metal using wafer bonding and subsequent selective substrate removal [7, 8, 19]. However, this approach has several drawbacks. First, it results in a considerable fabrication complexity. Second, it cannot be applied to all materials systems; in particular, it would be extremely challenging to apply this fabrication method to create nonlinear metasurfaces based on GaN/AlGaN heterostructures [14] grown on sapphire substrates. The GaN/AlGaN materials system offers very high conduction band offsets and may enable the extension of the operation range of the nonlinear intersubband polaritonic metasurfaces to the near-infrared regime ($\lambda \approx 0.7\text{--}3\ \mu\text{m}$) [14, 20, 21]. Finally, the metal ground plane prevents operation of the nonlinear polaritonic metasurfaces in transmission mode, which is preferable for many experimental implementations. We note that nonlinear polaritonic metasurfaces made of nanoresonators without ground planes were also reported previously [13]; however, the lack of the ground plane leads to smaller FF and SH field enhancements, which result in a weaker nonlinear metasurface response as discussed further below.

Here, we report an SHG metasurface fabricated using an “incomplete-metal-backplane” process that is readily amenable to GaN/AlGaN heterostructures, and can operate both in transmission and reflection modes. Graphic perspectives and side-views of the full-metal-backplane [8] and the incomplete-metal-backplane structures are presented in Fig. 1a, b, respectively. The fabrication procedure of the incomplete-metal backplane design is vastly simplified when compared to the full-metal backplane design, with the epitaxially grown MQW wafer being first patterned and etched via electron-beam lithography and a reactive-ion etch process (using a SiN_x dielectric hard mask), before a gold layer is unidirectionally evaporated on the tops of the individual resonators as well as in the gaps in between adjacent unit cells. This approach preserves the index-guided mode confinement (and thus, field enhancement) offered by etched resonator volumes, while the metal deposited adjacent to the base of the resonators presents an effective approximation to a full-metal backplane, resulting in a uniform field distribution and high field enhancement in the nanoresonator.

2 Metasurface design

To evaluate the efficiency of this novel incomplete-metal backplane approach, we designed, fabricated, and tested two metasurface samples following the outlined full- and incomplete-metal-backplane strategies, using the same MQW heterostructure for both methods. The bandstructure of a single period of the MQW heterostructure showing relevant electron subbands is presented in Fig. 1c. It was designed to provide strong SH response at a pump wavelength of $10\ \mu\text{m}$ (roughly 124 meV photon energy), and is similar to one reported in our prior work [8]. Unlike a doubly resonant design (where $E_{12} = E_{23} = E_{13}/2$), the 1–2 transition is purposefully detuned by approximately 25 meV from the FF energy to avoid the excessive optical losses at pump frequency and to delay the onset of intensity saturation of the nonlinear optical response [8, 19]. The 1–3 transition stays in resonance with the SH frequency to maintain large nonlinear optical response. The resulting design consists of 26 periods of an $\text{In}_{0.53}\text{Ga}_{0.47}\text{As}/\text{Al}_{0.52}\text{In}_{0.48}\text{As}$ structure with the layer sequence (in nm, and $\text{Al}_{0.52}\text{In}_{0.48}\text{As}$ barriers in bold) **2.5/6.2/1.4/2.4/2.5**, and was grown via a molecular beam epitaxy (MBE) process. The first 1.5 nm of the first 2.5 nm barrier and the last 1.5 nm of the last 2.5 nm barrier are n-doped to $7.3 \times 10^{18}\ \text{cm}^{-3}$, where we increased the dopant concentration by roughly 20% compared with the structure in our previous work [8], as $\chi_{\text{MQW},zzz}^{(2)}$ is expected to scale with the average bulk doping density [10, 22]. The MBE growth was carried out on a double-side polished semi-insulating InP wafer, starting with a 300 nm $\text{In}_{0.53}\text{Ga}_{0.47}\text{As}$ and 100 nm-thick InP etch stop layers (included for the full-metal-backplane process), followed by the 390 nm MQW region.

The intersubband absorption spectrum of the produced MQW heterostructure was obtained in a single-pass total-internal-reflection geometry, where the epi-side of the MQW wafer is sandwiched against a Ge prism, and light from a Fourier transform infrared (FTIR) source is directed through the prism at an angle beyond the critical angle at the Ge–MQW interface (approximately 60° from normal). We can attribute any reflectance dips in the spectrum of the signal for p-polarized incident light compared with s-polarized light to intersubband absorption within the MQW layer, noting again that the selection rules for the intersubband absorption only permit light with polarization components parallel to the growth direction to be absorbed. Following this method, we obtain $E_{12} = 140\ \text{meV}$ and $E_{13} = 235\ \text{meV}$, with full-width at half-maximum (FWHM) transition linewidths of 28 and 36 meV, respectively. We note a slight peak shift in the transition energies of the present structure from the identical MQW structure (20% lower doped) reported previously [8], which we attribute mostly to deviations in growth calibration at their respective times of

fabrication. Considering the transition energies, dipole moments, linewidths, and carrier concentration allows us to estimate the nonlinearity, $\chi_{\text{MQW},zzz}^{(2)}$, of the MQW, which we plot in Fig. 1d, and peaks at a pump wavelength of 10.45 μm , with $\chi_{\text{MQW},zzz}^{(2)} \approx 2.85 \times 10^5 \text{ pm} \cdot \text{V}^{-1}$.

It can be shown [7] that the relationship between the extrinsic susceptibility of the coupled polaritonic metasurface system and the intrinsic susceptibility of the MQWs alone can be encapsulated in the following equation for SHG, derived via Lorentz reciprocity:

$$\chi_{ijk}^{(2)} = \chi_{\text{MQW},zzz}^{(2)} \frac{\int_{\text{UC}} \xi_i^{2\omega}(x, y, z) \xi_j^{\omega}(x, y, z) \xi_k^{\omega}(x, y, z) dV}{V}, \quad (1)$$

where the second-order susceptibility tensor element $\chi_{ijk}^{(2)}$ ($i, j, k = x, y, \text{ or } z$) of the metasurface is related to the intrinsic susceptibility of the MQW, $\chi_{\text{MQW},zzz}^{(2)}$, by a volume-averaged overlap integral of the product of the local enhancement of the induced z -polarized E -field in the MQW. Here, $\xi_j^{\omega}(\xi_i^{2\omega})$ is the local enhancement of the induced z -polarized E -field in the MQW structure normalized to the $j(i)$ -polarized incident wave ω (2ω), and the integration occurs over the entire unit cell of volume V . Importantly, by virtue of this electromagnetic overlap integral, the metasurface unit cell can be designed to exhibit an effective susceptibility that significantly exceeds that of the MQW alone. This overlap integral also encapsulates the symmetry and geometric considerations inherent to a nanoresonator design suited for an efficient second-order nonlinear optical process. We found that etching the resonators by removing MQW volume surrounding the metal antenna serves to further confine and localize the plasmonic modes due to the index contrast of the MQW and surrounding free-space, resulting in an increased polarization response due to the stronger field enhancement, and larger nonlinear conversion efficiencies. This approach can also be exploited for individual control and decoupling of the local phase of neighboring nanoresonators, enabling continuous phase control of the nonlinearly generated beam at the individual nanoresonator level [9, 15].

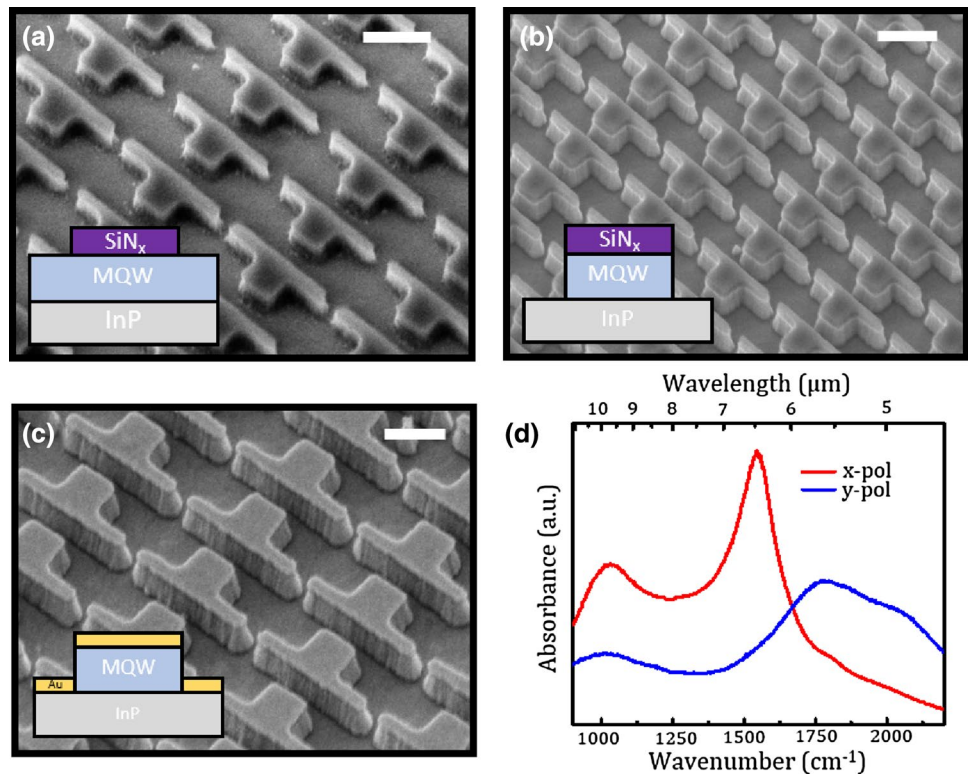
The resonator geometries for both full-metal and incomplete-metal backplane processes were optimized using a commercially available frequency-domain Maxwell's equations solver, with the goal of maximizing the calculated overlap integral for a given unit cell geometry. Figure 2a, c plots the z -polarized electric field contributions on an x - y -plane 200 nm beneath the top gold layer at fundamental and second harmonic wavelengths of 10.45 and 5.23 μm for the full and incomplete-metal backplane structures with dimensions given in Fig. 1a, b. The etched T geometry supports independently tuned cross-polarized resonances along the x -direction in the long arm at the FF, and y -direction in

the short arm at the SH frequency, correlating to a strong effective $\chi_{yxx}^{(2)}$ response. Figure 2b, d shows the electric field enhancement in the x - z -plane at a cross section along the x -directed long arm at the FF for full- and incomplete-backplane structures. Importantly, the field enhancement factors and spatial E_z distribution are comparable in magnitude for both designs. This is especially intriguing in the case of the incomplete-backplane design as there is no metal underneath the QW, and the metal deposited to the sides of the etched MQW volumes seems to serve as an adequate substitute for a complete-metal backplane. From our simulations, we calculate the volume-averaged overlap integrals from Eq. 1 to be and 3.4 and 1.1 for the full-metal and incomplete-metal backplane designs, respectively, correlating to $\chi_{yxx}^{(2)} \approx 9.7 \times 10^5 \text{ pm V}^{-1}$ and $3.1 \times 10^5 \text{ pm V}^{-1}$. All the other nonlinear susceptibilities are computed to be at least an order of magnitude smaller than these two components for the two metasurfaces, respectively.

As we mentioned previously, nanoresonators without a metal ground plane result in relatively low field enhancements [13] that lead to small values of the overlap integral. We have verified this point by computing the overlap integrals for the optimized T-shaped nanoresonators fabricated on top of InP substrate without using any metal backplane (complete or incomplete). The obtained values are 0.16 and 0.1 for the etched and non-etched T-shaped resonators with top metallization only, respectively. These values are much smaller than that obtained for the structures with the metal backplanes.

Fabrication of the full-metal backplane structure was carried out as described previously, starting with a 100-nm-thick gold deposition for the creation of the backplane, thermo-compressive wafer bonding to a separate InP substrate with an equivalent-thickness gold layer, and MQW substrate removal via mechanical polishing and selective wet etching. 50 nm of Au was then deposited by an electron-beam evaporation process to form the layer on top of the resonators, following which approximately 200 nm of a SiN_x hard mask was grown by a plasma-enhanced chemical vapor deposition process. The SiN_x was then patterned by electron-beam lithography and a reactive-ion etch process into a $300 \mu\text{m} \times 300 \mu\text{m}$ array of resonators with dimensions given in Fig. 1a. Finally, the metal-QW stack underneath the SiN_x was etched to form the individual QW resonator cavities by an inductively coupled reactive-ion-etch (ICP-RIE) process, and the SiN_x was selectively removed in a wet etch step. In contrast, fabrication of the incomplete-metal backplane structure is much less complicated, with schematic depictions of each step given in Fig. 3a–c, alongside scanning electron microscope images of the sample at each step. Approximately 200 nm of SiN_x was first deposited and patterned on a bare QW wafer, followed by electron-beam lithography and definition of the resonator geometry in SiN_x

Fig. 3 **a–c** Perspective scanning electron microscope images (rotated in-plane by 45° and tilted 30° from normal) of the intermediate steps in fabrication of an incomplete-metal-backplane SHG metasurface. The inset graphic depicts a side view of the material stack present in each step. **a** Image of the SiN_x dielectric hard mask used to etch the MQWs following an electron-beam lithography step. **b** Image of the MQW nanoresonators capped with SiN_x following an inductively coupled plasma etch. **c** Image of the fabricated metasurface following removal of the SiN_x hard mask and gold evaporation formation of the incomplete-metal backplane and plasmonic-cap. **d** Linear absorption spectra for *x*- and *y*-polarized light (red and blue curves, respectively) of the fabricated incomplete-metal-backplane metasurface



(dimensions given in Fig. 1b). An ICP-RIE process was then used to define the QW nanocavities using SiN_x as a dielectric hard mask. Finally, the SiN_x was selectively removed, and the incomplete-metal backplane and top gold were simultaneously created by a single 50-nm-thick evaporation of Au at normal incidence. The spectral and reflectance response of the nanoresonator antennas was determined from a reflectance measurement in a FTIR microscope system for incident *x*- and *y*- polarized light and given in Fig. 3d, where we note strong absorption resonances at the FF and SH frequencies of 955 and 1910 cm⁻¹, in agreement with our numerical simulations.

3 Metasurface characterization

Neglecting the pump depletion due to frequency conversion, the SHG intensity $I_{2\omega}$ is given as follows [10]:

$$I_{2\omega} = \frac{(2\omega)^2}{8\epsilon_0 c^3} |\chi_{yxx}^{(2)}|^2 I_{\omega}^2 d^2, \quad (2)$$

where $d \approx 400$ nm is the thickness of the nonlinear MQW region, 2ω is the SH frequency, and I_{ω} is the FF field intensity, and we assumed the FF beam to be polarized along *x*-direction and the SH beam to be polarized along *y*-direction (cf. Fig. 1 or Fig. 2). In our analysis below, we also

assume a Gaussian beam intensity distribution in the FF and SH waves, with the FF beam given as follows:

$$I_{\omega}(x, y) = I_{\omega}^0 \times \text{Exp}\left(-2 \frac{(x^2 + y^2)}{w_0^2}\right), \quad (3)$$

and the SH beam described as

$$I_{2\omega}(x, y) = I_{2\omega}^0 \times \text{Exp}\left(-4 \frac{(x^2 + y^2)}{w_0^2}\right). \quad (4)$$

We experimentally characterized the nonlinear response of both metasurfaces in a reflection configuration using the experimental set-up described in Fig. 4a. Normally incident light from a wavelength-tunable quantum-cascade laser (QCL, Daylight Solutions, Inc.) operating in pulsed mode (250 kHz repetition rate with 400-ns pulse width) is tuned to the MQW nonlinearity peak at 10.45 μm and focused onto the metasurface by a collimating lens (NA=0.5, with focal spot diameter $2w_0 = 35$ μm measured by the knife-edge technique) after passing through a half-wavelength-plate for polarization control and a long-wavelength-pass filter with transmission cutoff below the FF light operating as a beam splitter. The reflected SH light is discriminated from the pump by a ZnSe wire-grid linear polarizer to pass the *y*-polarized SH light and block the *x*-polarized FF and a short-wavelength-pass filter with a wavelength cutoff

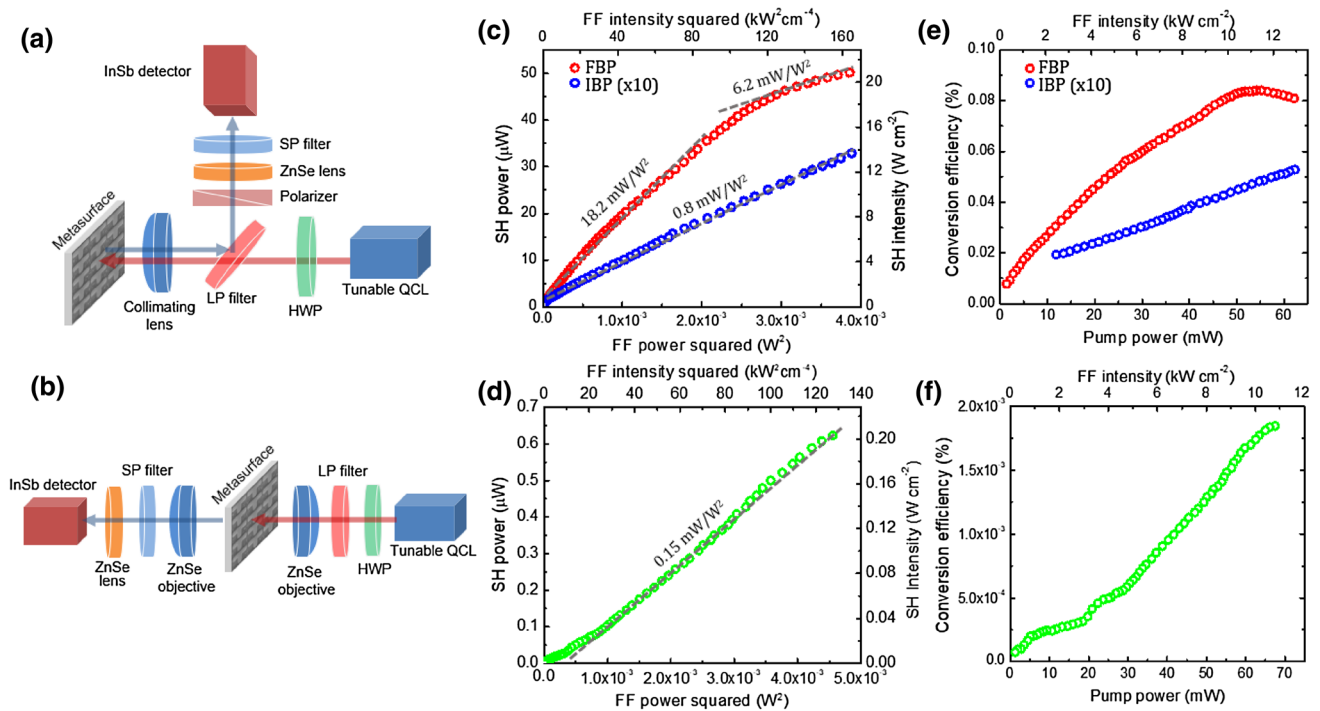


Fig. 4 Experimental optical set-ups and characterization results of the full- and incomplete-metal backplane SHG metasurfaces. **a** Optical set-up for characterization of the metasurfaces in a reflection configuration. Linearly polarized light from a tunable quantum-cascade laser (QCL) passes through an achromatic half-wave plate (HWP), a long-wavelength pass dichroic beam splitter (LP), and collimating lens to the sample. The reflected SHG light is redirected towards an InSb detector via a ZnSe wire-grid linear polarizer (LP) and short-wavelength pass filter (SP). **b** Optical set-up for the metasurface SHG characterization in a transmission configuration. Here, the light from the QCL is directed to a metasurface through an HWP, an LP filter, and a ZnSe objective. An identical objective is placed on the backside of the sample to collect the transmitted SHG light and direct it to the InSb detector through a SP filter. **c** SH power (left axis) and intensity (right axis) as a function of the FF pump power squared

(bottom axis) and intensity squared (top axis) for reflection measurements of the full-metal backplane (FBP, red circles) and incomplete-metal backplane (IBP, blue circles) metasurfaces. The measurements are performed at the pump wavelength of $10.45 \mu\text{m}$ and y_{xx} polarization combination. The data for the IBP is multiplied by a factor of 10, so that the same power and intensity scale bar can be used for both IBP and FBP data. **d** SH power (left axis) and intensity (right axis) as a function of the pump power squared (bottom axis) and intensity squared (top axis) for transmission measurements of the IBP metasurface. **e** SHG conversion efficiency as a function of FF pump power (bottom axis) and intensity (top axis) for the FBP (red circles) and IBP (blue circles) obtained from the data shown in (c), with the IBP data again scaled by a factor of 10. **f** Conversion efficiency in a function of FF power (bottom axis) and intensity (top axis) for the IBP in transmission mode from the data in (d)

below the FF light. The SH light is focused onto a calibrated, liquid-nitrogen cooled InSb detector, and the reflected SH power is recorded as a function of input intensity, after being corrected for the power loss over the optical path. The lack of a full-metal backplane beneath the resonators in the incomplete-metal design also allows for illumination and measurement in a transmission configuration, as depicted in Fig. 4b. Here, the set-up is largely similar to the reflection configuration, but instead of employing a single collimating lens for focusing of the FF light and collection of the SH, we use two identical ZnSe objectives (NA = 0.25, with focal spot diameter $2w_0 = 40 \mu\text{m}$) for focusing of the FF light onto the sample and collection of the generated SH.

These results for the full- and incomplete-metal backplane samples are given in Fig. 4c, d, for reflection and transmission modes, respectively. The reflection data in Fig. 4c were corrected for the optical transmission of our set-up,

and the data for SHG power in transmission mode in Fig. 4d were corrected for both the optics transmission (97.5% for the ZnSe objective, 85% for the short-wavelength pass filter, and 90% for the ZnSe lens) and the Fresnel reflection (26%) of the generated SH signal at the InP -air interface in the incomplete-metal backplane sample. The reflection loss at the InP -air interface can, in principle, be reduced to nearly zero by introduction of an anti-reflection coating for SH light.

In Fig. 4e, we plot the conversion efficiency for the peak intensities of the FF and SH Gaussian beams defined as $\eta = \frac{P_{2\omega}^0}{P_{\omega}^0} = \frac{I_{2\omega}^0}{2I_{\omega}^0}$ [cf. Eqs. (2), (3), and (4)] for the full- and incomplete-metal backplane samples operating in reflection mode. From Fig. 4e, we note that we achieve approximately 0.083% SH conversion efficiency at a pump intensity of only 10 kW/cm^2 for the full-metal backplane sample and 0.01%

for the incomplete-metal backplane. Figure 4f depicts the measured conversion efficiencies in transmission mode, where we observe a conversion efficiency of $1.8\text{e-}3\%$ for the incomplete-metal backplane sample at an intensity of 11 kW/cm^2 . From the quadratic dependence of the SHG intensity on the pump intensity in Eq. (2), we expect a linear increase in η with the pump intensity. However, due to optical saturation of the 1–2 intersubband transition for high incident powers, the conversion efficiency experiences saturation, as shown in Fig. 4e. The effect is particularly strong in the case of the complete-metal-backplane due to strong field enhancement in the nanoresonators. From these conversion efficiency values, we can deduce the metasurface nonlinearity using Eq. (2). We obtain $\chi_{yxx}^{(2)}$, of $1.54 \times 10^6\text{ pm V}^{-1}$ for low-intensity excitation of the full-backplane sample and $3.27 \times 10^5\text{ pm V}^{-1}$ for the incomplete-backplane sample in reflection geometry. Both are within reasonable agreement with our theoretically predicted values, and orders of magnitude larger than values achievable in traditionally used nonlinear crystals [10, 16]. At higher pumping intensities $\sim 10\text{ kW/cm}^2$, the value $\chi_{yxx}^{(2)}$ becomes $9.37 \times 10^5\text{ pm V}^{-1}$ for the full-backplane sample, while we do not observe any significant onset of intensity saturation in the incomplete-backplane sample, which is due to the lower field enhancement in the nanoresonator for the latter case.

The results indicate that the incomplete-metal-backplane intersubband polaritonic metasurface design can offer a viable alternative to the full-metal-backplane design, particularly for higher pumping intensities. The incomplete-backplane metasurface also possesses an effective nonlinear response in the transmission geometry, with $\chi_{yxx}^{(2)} \sim 4.21 \times 10^4\text{ pm V}^{-1}$. We also note that the value of $\chi_{yxx}^{(2)}$ for the full-backplane sample corresponds to a roughly 10% improvement over our previous record [8], and represents the new record for second-order nonlinearity in the IR–visible range for a condensed matter system. The observed improvement over our previous work could be due to several factors, including employment of a slightly different, better optimized resonator design, and a higher quality fabrication. Finally, we stress that further improvements to resonator and MQW design and fabrication could potentially lead to further significant advancements over our presented results [8, 19].

4 Conclusion

In summary, we have presented the design, fabrication, and experimental operation of an SHG metasurface based on coupling electromagnetic modes in plasmonic nanoresonator-to-intersubband transitions in the MQW heterostructures using a nanoresonator design that does not require the formation of a metal backplane. The metasurface design is suitable for operation in transmission mode and it can be implemented

with III-nitride MQWs where processes for selective substrate removal are challenging to implement. Our results show a roughly four times reduction in the overall nonlinearity of the incomplete-backplane design compared to the full-backplane design at pumping intensities $\sim 10\text{ kW/cm}^2$.

Acknowledgements Parts of this work were supported by the U.S. Department of Energy, Office of Basic Energy Sciences, Division of Materials Sciences and Engineering and performed, in part, at the Center for Integrated Nanotechnologies, an Office of Science User Facility operated for the U.S. Department of Energy (DOE) Office of Science. Sandia National Laboratories is a multi-mission laboratory managed and operated by National Technology and Engineering Solutions of Sandia, LLC, a wholly owned subsidiary of Honeywell International, Inc., for the U.S. Department of Energy's National Nuclear Security Administration under contract DE-NA0003525.

References

1. B. Corcoran, C. Monat, C. Grillet, D.J. Moss, B.J. Eggleton, T.P. White, L. O'Faolain, T.F. Krauss, *Nat. Photonics* **3**, 206 (2009)
2. C. Wang, Z. Li, M.H. Kim, X. Xiong, X.F. Ren, G.C. Guo, N. Yu, M. Lončar, *Nat. Commun.* **8**, (2017)
3. P.S. Kuo, J. Bravo-Abad, G.S. Solomon, *Nat. Commun.* **5**, (2014)
4. M. Celebrano, X. Wu, M. Baselli, S. Großmann, P. Biagioni, A. Locatelli, C. De Angelis, G. Cerullo, R. Osellame, B. Hecht, L. Duò, F. Ciccacci, M. Finazzi, *Nat. Nanotechnol.* **10**, 412 (2015)
5. N. Yu, F. Capasso, *Nat. Mater.* **13**, 139 (2014)
6. A.V. Kildishev, A. Boltasseva, V.M. Shalae, *Science* **339**, 1289 (2013)
7. J. Lee, M. Tymchenko, C. Argyropoulos, P.-Y. Chen, F. Lu, F. Demmerle, G. Boehm, M.-C. Amann, A. Alù, M.A. Belkin, *Nature* **511**, 65 (2014)
8. J. Lee, N. Nookala, J.S. Gomez-Diaz, M. Tymchenko, F. Demmerle, G. Boehm, M.-C. Amann, A. Alù, M.A. Belkin, *Adv. Opt. Mater.* **4**, 664 (2016)
9. N. Nookala, J. Lee, M. Tymchenko, J. Sebastian Gomez-Diaz, F. Demmerle, G. Boehm, K. Lai, G. Shvets, M.-C. Amann, A. Alù, M.A. Belkin, *Optica* **3**, 283 (2016)
10. R.W. Boyd, *Nonlinear Optics* (Academic Press, New York, 2008)
11. G. Li, S. Chen, N. Pholchai, B. Reineke, P.W.H. Wong, E.Y.B. Pun, K.W. Cheah, T. Zentgraf, S. Zhang, *Nat. Mater.* **14**, 607 (2015)
12. N. Segal, S. Keren-Zur, N. Hendler, T. Ellenbogen, *Nat. Photonics* **9**, 180 (2015)
13. O. Wolf, S. Campione, A. Benz, A.P. Ravikumar, S. Liu, T.S. Luk, E.A. Kadlec, E.A. Shaner, J.F. Klem, M.B. Sinclair, I. Brener, *Nat. Commun.* **6**, 7667 (2015)
14. O. Wolf, A.A. Allerman, X. Ma, J.R. Wendt, A.Y. Song, E.A. Shaner, I. Brener, *Appl. Phys. Lett.* **107**, 151108 (2015)
15. M. Tymchenko, J.S. Gomez-Diaz, J. Lee, N. Nookala, M.A. Belkin, A. Alù, *Phys. Rev. Lett.* **115**, 207403 (2015)
16. Y.R. Shen, *The Principles of Nonlinear Optics* (Wiley-Interscience, New York, 2002)
17. F.B.P. Niesler, N. Feth, S. Linden, J. Niegemann, J. Gieseler, K. Busch, M. Wegener, *Opt. Lett.* **34**, 1997 (2009)
18. W. Fan, S. Zhang, K.J. Malloy, S.R.J. Brueck, N.C. Panou, R.M. Osgood, *Opt. Express* **14**, 9570 (2006)
19. J.S. Gomez-Diaz, M. Tymchenko, J. Lee, M.A. Belkin, A. Alù, *Phys. Rev. B* **92**, 125429 (2015)
20. I. Vurgaftman, J.R. Meyer, *J. Appl. Phys.* **94**, 3675 (2003)
21. M. Beeler, E. Trichas, E. Monroy, *Semicond. Sci. Technol.* **28**, 74022 (2013)
22. E. Rosencher, A. Fiore, B. Vinter, V. Berger, P. Bois, J. Nagle, *Science* **271**, 168 (1996)